New Journal of Physics
The open-access journal for physics

Local Hanle-effect studies of spin drift and diffusion in n:GaAs epilayers and spin-transport devices

M Furis[1,5], D L Smith[2], S Kos[2,6], E S Garlid[3], K S M Reddy[4], C J Palmstrøm[4], P A Crowell[3] and S A Crooker[1,7]

[1] National High Magnetic Field Laboratory, Los Alamos, NM 87545, USA
[2] Theoretical Division, Los Alamos National Laboratory, Los Alamos, NM 87545, USA
[3] School of Physics and Astronomy, University of Minnesota, Minneapolis, MN 55455, USA
[4] Department of Chemical Engineering and Materials Science, University of Minnesota, Minneapolis, MN 55455, USA
E-mail: crooker@lanl.gov

New Journal of Physics **9** (2007) 347
Received 16 May 2007
Published 28 September 2007
Online at http://www.njp.org/
doi:10.1088/1367-2630/9/9/347

Abstract. In electron-doped GaAs, we use scanning Kerr-rotation microscopy to locally probe and spatially resolve the depolarization of electron spin distributions by transverse magnetic fields. The shape of these local Hanle-effect curves provides a measure of the spin lifetime as well as spin transport parameters including drift velocity, mobility and diffusion length. Asymmetries in the local Hanle data can be used to reveal and map out the effective magnetic fields due to spin–orbit coupling. Finally, using both spin imaging and local Hanle effect studies, we investigate the drift and diffusion of electrically-injected spins in lateral Fe/GaAs spin-detection devices, both within and outside the current path.

[5] Present address: Department of Physics, University of Vermont, Burlington, VT 05405, USA.
[6] Present address: Cavendish Laboratory, JJ Thomson Ave, Cambridge CB3 0HE, UK.
[7] Author to whom any correspondence should be addressed.

PII: S1367-2630(07)50586-0

Contents

1. Introduction

A number of prototype 'semiconductor spintronic' devices have been fabricated in recent years, including spin-polarized light-emitting diodes [1]–[7], tunnel junctions [8], and ferromagnet/semiconductor spin injection and detection devices [9]–[12]. Their functionality is based, in whole or in part, on means for electrical spin injection, transport, manipulation and detection [13]. From a design point of view, knowledge of how the spin transport parameters (including spin lifetime, diffusion and mobility) depend on doping, bias, temperature, strain and geometry are of critical importance. Often these parameters are difficult to infer from electrical measurements alone. Optical techniques provide a powerful, alternate means of probing spin-polarized electrons [10], [14]–[17]. For example, optical Hanle-effect studies of electron depolarization by a transverse magnetic field have been used for decades to determine spin lifetimes in zincblende and wurtzite semiconductors [18].

In this paper, we describe a series of 'local Hanle effect' measurements in n:GaAs using a focused, scanning optical probe to measure and spatially resolve the details of electron depolarization. Together with direct spin imaging based on the Kerr effect and numerical modeling, these local Hanle data reveal not only the spin lifetime but also the spin diffusion constant, drift velocity and mobility. In low-doped n:GaAs ($n_e = 0.4$–$5\times10^{16}\,\mathrm{cm}^{-3}$), where the electron spin transport lengths routinely exceed 10 μm [19, 20], a local optical probe measures only a subset of spins from the overall, spatially-extended spin distribution. This subset can have a well-defined average momentum and 'age' that is quite different from that of the whole ensemble. In this way, the shape of these local Hanle data can reveal transport parameters. Further, the effects of spin–orbit coupling can manifest directly as asymmetries in local Hanle data, as demonstrated here for a spin–orbit coupling due to applied uniaxial strain. Finally, we show that local Hanle studies provide details of spin diffusion and transport in Fe/GaAs semiconductor spin injection and detection devices, both within and outside the current path.

2. Scanning Kerr-rotation microscopy and the local Hanle effect

Figure 1 shows a schematic of the experiment. Semiconductor samples are mounted strain-free on the vacuum cold finger of a small optical cryostat, which in turn is mounted on

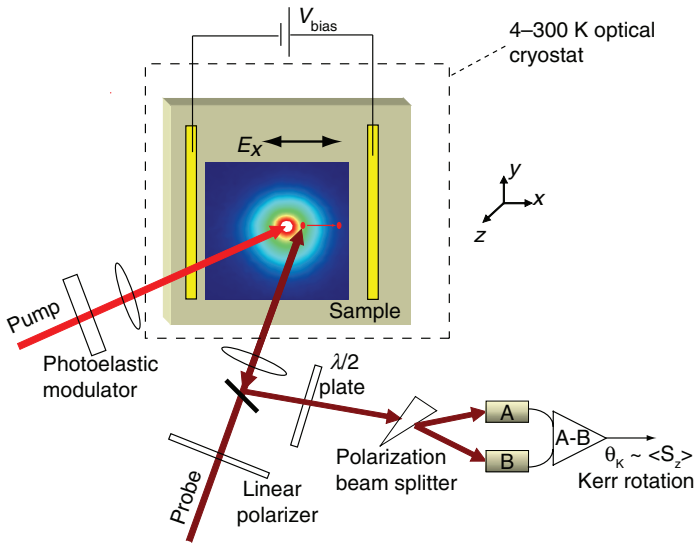

Figure 1. Experimental schematic. Spin-polarized electrons are optically injected into semiconductors with a separate pump laser (as shown), or electrically injected from ferromagnetic contacts. The polar Kerr rotation (θ_K) imparted on the reflected probe laser is proportional to S_z, the out-of-plane electron spin component. Local Hanle-effect data are obtained by fixing the focused probe laser at a particular spot and sweeping a transverse magnetic field ($B_{x,y}$) using external coils.

a x–y positioning stage. The out-of-plane component of electron spin polarization in the semiconductor, S_z, is measured at a particular location via the polar Kerr rotation θ_K imparted on a linearly-polarized probe laser that is focused on (and reflected from) the sample at normal incidence. The probe beam ($<100\,\mu$W) is derived from a narrow-band continuous-wave Ti:sapphire ring laser, which is typically tuned just below the semiconductor bandgap. The probe focusing lens is also mounted on a positioning stage, and two-dimensional images of S_z are obtained by raster-scanning either the cryostat or (more typically) the probe focusing lens.

To study optically-injected spins, a separate above-bandgap cw pump laser is also focused on the sample. The polarization of the pump laser can be modulated from right- to left-circular (injecting spins along $\pm\hat{z}$) at 50 kHz using a photoelastic modulator. In this way the purely spin-dependent Kerr response is readily measured with lock-in techniques, and nuclear spin pumping effects are mitigated. When using both probe and pump lasers, space considerations limit the numerical apertures of the focusing optics. Generally, both beams can be focused to 4–5 μm diameter spots.

Electrically-injected spins are studied using the probe laser alone, by modulating the applied voltage bias at kilohertz frequencies. Electrically-injected spins have an initial orientation in the x–y sample plane (e.g. along a contact magnetization), and therefore external magnetic fields are required to tip (precess) these spins to an out-of-plane direction ($\pm\hat{z}$) where they can be measured by the polar Kerr effect. External coils (not drawn) control the applied fields B_x, B_y and B_z. These coils are also used together with the local probe beam to study the depolarization and dephasing of spins by applied transverse magnetic fields—the 'local Hanle'

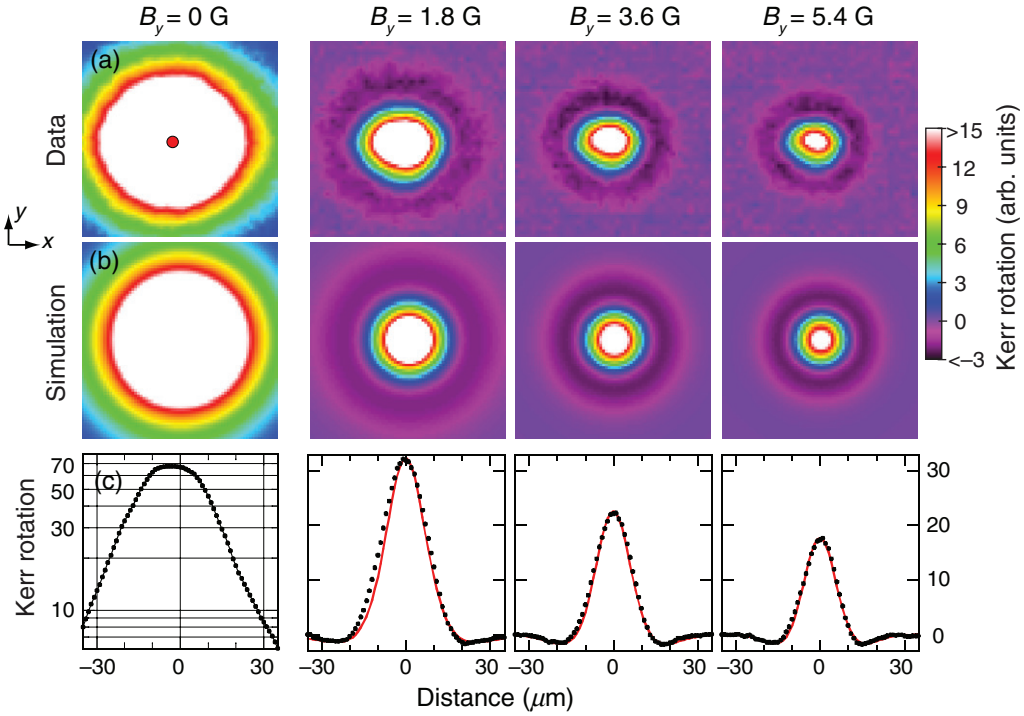

Figure 2. Imaging and modeling the radial diffusion of optically-injected electron spins in a n:GaAs epilayer at 10 K ($n_e = 4 \times 10^{15}$ cm^{-3}, 15 μm thick). (a) 70×70 μm image of the measured Kerr rotation ($\theta_K \propto S_z$) in zero magnetic field. The red dot shows the 5 μm diameter of the focused injection laser. Subsequent images are acquired in transverse fields $B_y = 1.8$, 3.6 and 5.4 G. Purple and black colors (see scale) indicate negative signal, or spins that have precessed from $+\hat{z}$ into $-\hat{z}$. (b) Simulations of S_z at the same fields using $\tau_s = 600$ ns and $D = 3.5$ cm^2 s^{-1}. (c) Line-cuts through the data (black points) and the simulations (red lines). The case of $B_y = 0$ is shown on a log scale.

effect. In these studies, S_z from the probed spins (a subset of the total spin distribution) is measured as a function of B_x or B_y.

3. Imaging and modeling 2D spin diffusion in n:GaAs epilayers

Figure 2(a) shows a 70×70 μm Kerr-rotation image of the electron spin polarization, S_z, resulting from optical spin injection into a n:GaAs bulk epilayer at 10 K and in zero magnetic field. The weak pump laser (5 μW) is focused to a 5 μm diameter spot (shown by the red dot), and injected spins diffuse radially away from the point of injection in the x–y plane. The large spatial extent of this 'spin cloud' is set by the spin diffusion length, $L_s = \sqrt{D\tau_s}$, where D and τ_s are the electron diffusion constant and spin lifetime (spin diffusion in these bulk epilayers is well-approximated by charge diffusion, in contrast to high-mobility heterostructures [16]). A line-cut through the data (figure 2(c)) shows that S_z decays nearly exponentially at large distance, with a decay length of ∼13 μm.

Spin drift and diffusion in these n:GaAs epilayers can be treated in 2D because the epilayers are, in general, thinner than L_s.[8] Thus, for the case of applied in-plane magnetic and electric fields ($B_{x,y}$, $E_{x,y}$), the steady-state spin polarization $\mathbf{S}(\mathbf{r})$ can be derived from the 2D drift-diffusion equation:

$$\partial\mathbf{S}/\partial t = D\nabla_{\mathbf{r}}^2\mathbf{S} + \mu(\mathbf{E}\cdot\nabla_{\mathbf{r}})\mathbf{S} + g\mu_B\hbar^{-1}(\mathbf{B}\times\mathbf{S}) - \mathbf{S}/\tau_s + \mathbf{G}(\mathbf{r}) = 0, \tag{1}$$

here, $\mathbf{G}(\mathbf{r})$ is a generation term ($= G_z(\mathbf{r})$ for optical spin injection), μ is the electron mobility, μ_B is the Bohr magneton, and g is the electron g-factor ($g = -0.44$ in GaAs). The terms in (1) describe diffusion, drift, precession, relaxation and generation, respectively.

The simplest case of $\mathbf{B} = \mathbf{E} = 0$ applies directly to the data in figure 2(a). In this case, the Green's function solution (i.e. if $G_z(\mathbf{r})$ is a *point* source at the origin) is $S_z(\mathbf{r}) = (G_z/2\pi D)K_0(r/L_s)$, where K_0 is the zeroth-order modified Bessel function of the second kind and r is the distance from the injection point (this solution must be convolved with $\mathbf{G}(\mathbf{r})$ to obtain the actual steady-state spin distribution). For $r > L_s$, $K_0(r/L_s)$ falls nearly exponentially with a $1/e$ decay constant of $\sim 0.9L_s$. Therefore, the line-cut through figure 2(c) indicates that $L_s \simeq 13\,\mu\text{m}/0.9 \simeq 14.5\,\mu\text{m}$ in this epilayer at 10 K. Figure 2(b) shows the simulated 2D spin image, obtained using a 5 μm diameter gaussian injection spot, $\tau_s = 600$ ns and $D = 3.5\,\text{cm}^2\,\text{s}^{-1}$ (τ_s was measured independently in this epilayer, as discussed below).

The three spin images shown to the right of figure 2(a) were acquired in the presence of small transverse magnetic fields, $B_y = 1.8$, 3.6 and 5.4 G. B_y causes the injected spins to precess at their Larmor frequency $\omega_L = g\mu_B B_y/\hbar$. At a characteristic distance from the injection point the diffusing spins have, on an average, precessed from $+\hat{z}$ to $-\hat{z}$ (π radians), giving an annulus of oppositely-oriented spins (and negative signal) about the injection point as observed. This annulus shrinks when spins precess faster in larger B_y, as expected. Solving for $S_z(\mathbf{r})$ in the presence of electric and magnetic field yields the 2D Green's function solution:

$$S_z(\mathbf{r}) = \frac{G_z}{2\pi D}\exp\left(\frac{\mu\mathbf{E}\cdot\mathbf{r}}{2D}\right)\text{Re}\left[K_0\left(r\sqrt{\left(\frac{\mu E}{2D}\right)^2 + \frac{1}{D\tau_s} + \text{i}\left(\frac{g\mu_B B}{\hbar D}\right)}\right)\right], \tag{2}$$

where the imaginary part of the complex argument of K_0 generates oscillations due to spin precession. Taking $\mathbf{E} = 0$ and convolving $S_z(\mathbf{r})$ with the injection spot gives the simulated images to the right of figure 2(b), using $\tau_s = 600$ ns and $D = 3.5\,\text{cm}^2\,\text{s}^{-1}$. Figure 2(c) shows that line-cuts through the data and the simulations are in good agreement.

Alternatively, S_z can be numerically computed from a set of spin drift-diffusion equations in 2D. A fully numerical approach is often simplest, particularly when including spin–orbit coupling terms. For in-plane electric and magnetic fields, and for spin–orbit coupling due to off-diagonal strain in bulk GaAs, a full set of 2D spin drift-diffusion equations was presented in [20, 21], and are reproduced here for completeness. The three equations determining the steady-state spin densities $n_{x,y,z}(\mathbf{r})$ are $O_1 n_x + O_2 n_z = -G_x$, $O_1 n_y + O_3 n_z = -G_y$ and $O_4 n_z - O_2 n_x - O_3 n_y = -G_z$, where

$$O_1 = D\nabla_{\mathbf{r}}^2 + \mu\mathbf{E}\cdot\nabla_{\mathbf{r}} - C_s^2 D - 1/\tau_s, \tag{3}$$

$$O_2 = g\mu_B B_y/\hbar + C_s(2D\nabla_x + \mu E_x), \tag{4}$$

$$O_3 = -g\mu_B B_x/\hbar + C_s(2D\nabla_y + \mu E_y), \tag{5}$$

[8] In the $4\times10^{15}\,\text{cm}^{-3}$ epilayer, L_s and the thickness are comparable ($\simeq 15\,\mu$m).

$$O_4 = D\nabla_{\mathbf{r}}^2 + \mu\mathbf{E}\cdot\nabla_{\mathbf{r}} - 2C_s^2 D - 1/\tau_s. \quad (6)$$

$G_{x,y,z}(\mathbf{r})$ are source terms, and $C_s = C_3 m\epsilon_{xy}/\hbar^2$ is the spin–orbit term that couples spin to the off-diagonal elements of the strain tensor in GaAs, ϵ_{xy} [20, 22]. This spin–orbit coupling to strain generates effective magnetic fields with the same $\sigma_x k_y - \sigma_y k_x$ symmetry as the Rashba spin–orbit coupling common in heterostructures.

4. Spin depolarization in transverse magnetic fields: Hanle effect

The depolarization of an oriented spin ensemble by an applied transverse magnetic field is known as the Hanle effect [18]. In 'conventional' Hanle effect studies, a continuous-wave laser injects a steady-state population of spin-polarized carriers ($\mathbf{S_0} \parallel \hat{z}$), and S_z is monitored by the photoluminescence (PL) polarization as a function of transverse magnetic field (e.g. B_y). Spin precession at the Larmor frequency ω_L dephases (depolarizes) the spin ensemble, reducing S_z. Ignoring recombination effects[9], spins injected at time $t = 0$ decay and precess as $S_z(t) = S_0 \exp(-t/\tau_s)\cos(\omega_L t)$. If PL from the *entire* ensemble is measured (as is usually the case), then the average steady-state spin polarization is obtained by integrating over all injection times: $S_z(B_y) = S_0 \int_0^\infty e^{-t/\tau_s}\cos(\omega_L t)\,dt$. This expression gives the Lorentzian lineshape of conventional Hanle data, $S_z(B_y) = S_0/[1 + (g\mu_B B_y \tau_s/\hbar)^2]$, with half-width $B_{1/2} = \hbar/(g\mu_B\tau_s)$.

Alternatively, if only a specific *subset* of the total spin ensemble is detected, then S_z versus B_y will not, in general, exhibit a conventional Lorentzian lineshape. Rather, the lineshape will reveal the depolarization of only the detected spins, and this subset of spins may have a well-defined average momentum and 'age' that are quite different from that of the whole ensemble. This is precisely the situation realized with the scanning Kerr microscope and n:GaAs doped near the metal–insulator transition, where spin transport lengths routinely exceed the size of the local probe laser. At different locations on the sample, the focused probe laser selectively measures local subsets of the spatially-extended spin distribution. The depolarization of these subsets by transverse fields—a 'local Hanle' effect—reveals important spin transport properties.

Figure 3(a) shows conventional Hanle-effect studies of electron spin lifetime at 10 K in three n:GaAs epilayers with doping $n_e = 0.4$, 1 and $5 \times 10^{16}\,\mathrm{cm}^{-3}$. To satisfy the conditions for measuring a conventional Hanle effect, the pump laser beam was defocused to a large spot size ($>200\,\mu$m) that greatly exceeds L_s, and S_z was measured via the Kerr rotation imparted on the focused probe laser. Defocusing the pump laser ensures that the electrons diffusing under the probe spot are representative of the ensemble average and do not have a preferred momentum or effective 'age'. Using $g = -0.44$, the full-widths of these peaks are $2B_{1/2} \simeq 0.86$, 2.85 and 6.60 G, indicating that $\tau_s \simeq 600$, 180 and 78 ns in the 0.4, 1 and $5 \times 10^{16}\,\mathrm{cm}^{-3}$ epilayers at 10 K, respectively, in reasonable agreement with prior studies of spin relaxation in n:GaAs [23, 24]. Using these methods, it was recently shown that τ_s drops dramatically in n:GaAs at low temperatures when applied electric fields exceed $\sim 11\,\mathrm{V\,cm}^{-1}$, due to donor impact ionization [25].

Figure 3(b) shows the transition from a conventional Hanle effect to a local Hanle effect. Measuring S_z versus B_y in a 1 μm thick $n_e = 10^{16}\,\mathrm{cm}^{-3}$ epilayer while keeping the pump and probe overlapped, the diameter of the pump spot is reduced from 200 to 5 μm. $B_{1/2}$ increases dramatically when the pump diameter shrinks below L_s and is tightly focused. In this case $B_{1/2}$ no longer provides a direct measure of τ_s. Rather, the width is now determined primarily by

[9] This is a good approximation in n-type GaAs with weak optical pumping; see [23].

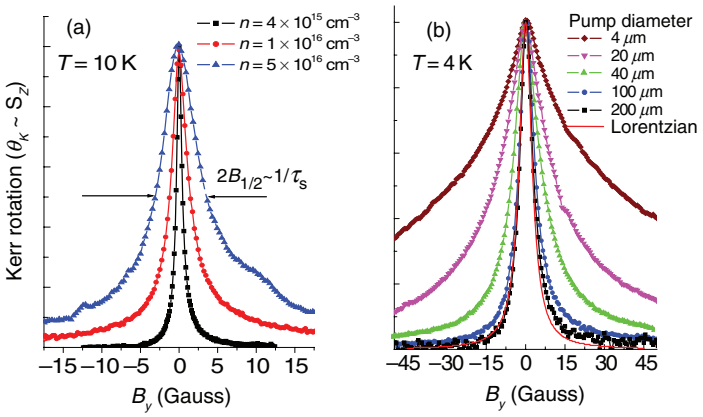

Figure 3. (a) Conventional Hanle effect (S_z versus B_y) measured in three n:GaAs epilayers at 10 K. The probe beam is focused to a 4 μm spot, and the diameter of the (defocused) pump spot, d, is much larger than the spin diffusion length L_s. In this limit, $B_{1/2} \propto \tau_s^{-1}$. (b) Hanle effect data in the $n_e = 1 \times 10^{16}\,\mathrm{cm}^{-3}$ epilayer as d is reduced. When $d < L_s$, $B_{1/2}$ increases dramatically as the probe now measures only a subset of the spin ensemble (a 'local Hanle' effect).

the (short) time required for the injected electrons to diffuse out from under the focused probe. Essentially, the local probe laser is measuring a subset of the injected spins that are relatively *young* in comparison to the entire ensemble. Local Hanle effect studies of spin sub-ensembles that have nonzero momentum, due to drift or due to diffusion alone, are treated in the next two sections.

5. Local Hanle effect measurements of drifting spins

The transport properties of spins drifting in an applied electric field E_x can be inferred from local Hanle effect measurements. Figure 4(a) shows an image of spins diffusing and drifting away from the point of optical injection in a lateral electric field $E_x = 10.5\,\mathrm{V\,cm}^{-1}$. Figure 4(b) shows the evolution of the local Hanle curves as the focused probe laser is scanned horizontally across this steady-state spin distribution in 4 μm steps.

Downstream of the injection spot the local Hanle curves become increasingly narrow, exhibiting multiple oscillations at large separations. The large drift velocity and spin lifetime allow access to a spatial regime far from the injection point (and well in excess of $\sqrt{D\tau_s}$) where the 'time-of-flight' required for electrons to reach the detection point roughly determines their average 'age'. For example, at $x = 56\,\mu$m, S_z crosses zero at $B_0 \simeq \pm 3.1$ G at which point the spins have precessed $\pm\pi/2$ radians, taking time $t = \pi/(2\omega_L) \simeq 130$ ns to do so. From these values a spin drift velocity $v_d = x/t \simeq 4.3 \times 10^4\,\mathrm{cm\,s}^{-1}$ can be estimated. This simple estimation is only approximate due to the 2D nature of the spin transport in this case. More accurate values of v_d (and also D and τ_s) are possible by simulating the Hanle data using the fully 2D analytic or numerical solutions described above. Figure 4(c) shows the numerically-simulated Hanle curves, using $D = 10\,\mathrm{cm}^2\,\mathrm{s}^{-1}$, $\tau_s = 150$ ns and $v_d = 4 \times 10^4\,\mathrm{cm\,s}^{-1}$.

It is also instructive to inspect the relevant integral solution for spin transport in 1D, which corresponds to the case of uniform spin injection along a vertical line in a 2D plane. Although

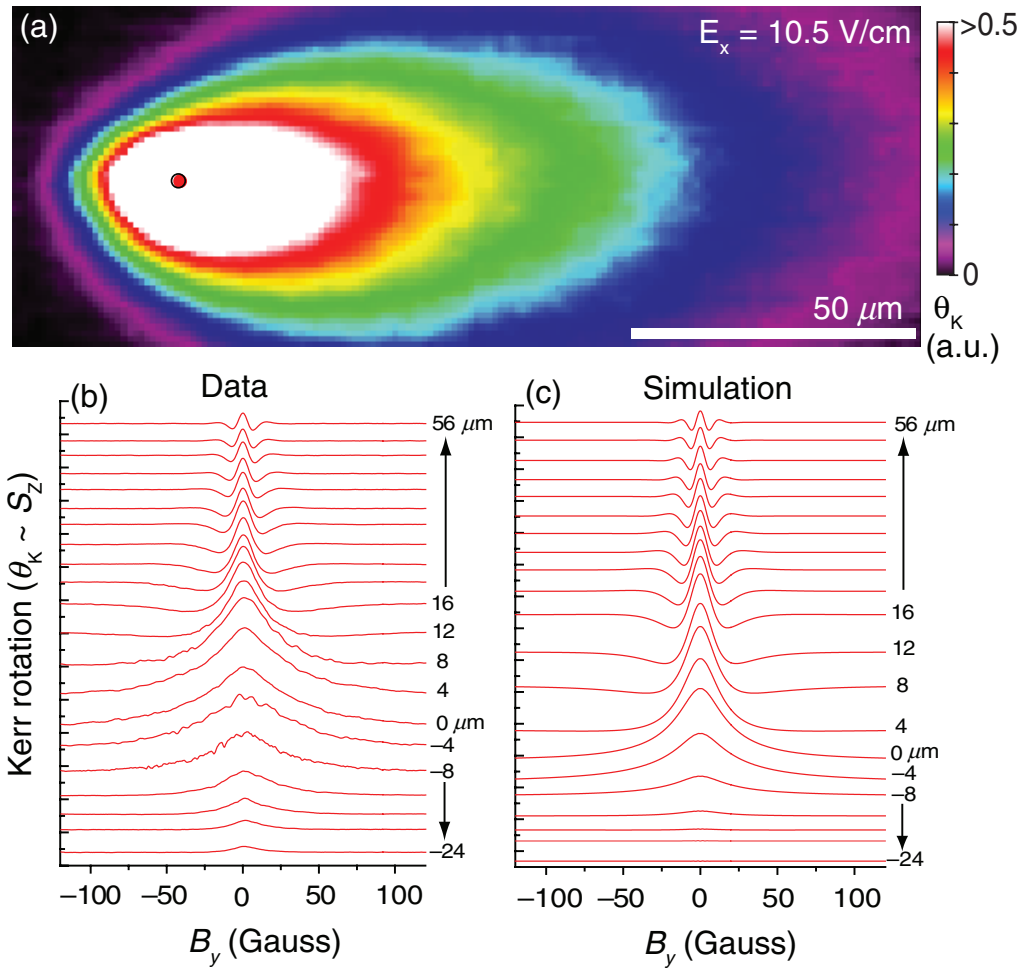

Figure 4. (a) An image of optically-injected electron spins diffusing and drifting in a lateral electric field ($E_x = 10.5\,\mathrm{V\,cm^{-1}}$) at 4 K in a $n = 1 \times 10^{16}\,\mathrm{cm^{-3}}$ n:GaAs epilayer (1 μm thick). The red dot denotes the injection spot. (b) Evolution of the local Hanle curves (S_z versus B_y) with distance to the right of the injection point. (c) Simulated data using the 2D spin drift-diffusion model ($D = 10\,\mathrm{cm^2\,s^{-1}}$, $\tau_s = 150$ ns and $v_d = \mu E_x = 4 \times 10^4\,\mathrm{cm\,s^{-1}}$).

not strictly accurate for the 2D drift and diffusion shown in figure 4, this integral solution approximates 2D spin transport in the limit that the spin drift length exceeds the diffusion length ($\mu E \tau_s > \sqrt{D\tau_s}$). At a distance x from a line-like source, $S_z(x, B_y)$ can be written as:

$$S_z(x, B_y) = \int_0^\infty \frac{S_0}{\sqrt{4\pi Dt}} e^{-(x - v_d t)^2/4Dt} e^{-t/\tau_s} \cos(\omega_L t)\, dt. \quad (7)$$

This expression is similar to the integral expression for the conventional Hanle effect described above, except that one must now integrate the spin orientation of the precessing electrons over the gaussian distribution of their arrival times at position x, which are smeared by diffusion. If the distribution of arrival times is narrowly peaked, prominent oscillations appear in local Hanle data. This corresponds to the 'time-of-flight' regime where $x > D/v_d$. Note that this 1D solution *does* accurately describe the largely 1D spin transport that occurs in lateral Fe/GaAs devices [10]–[12] (to be discussed).

6. Revealing spin–orbit effects with local Hanle measurements

In this section, we show how asymmetries in local Hanle measurements can provide a direct measure of spin–orbit effects in GaAs. Frequently suggested as a means of spin manipulation in 'semiconductor spintronic' device proposals, spin–orbit coupling of the generic form $\boldsymbol{\sigma} \cdot (\mathbf{k} \times \nabla V)$ generates effective magnetic fields that are 'seen' by carriers with momentum $\mathbf{k}$ in a non-uniform potential V. Bulk- and structural-inversion asymmetry of the underlying lattice are two common sources of spin–orbit coupling in semiconductors and their heterostructures (Dresselhaus and Rashba coupling, respectively). The direction and magnitude of their associated effective magnetic fields, $\mathbf{B}_{\text{eff}}$, explicitly depends on $\mathbf{k}$ [26, 27]. Thus, for 2D drift and diffusion in the sample plane, $\mathbf{B}_{\text{eff}}$ is not uniform and can depend strongly on position.

Local Hanle effect studies can directly reveal and spatially map the effective magnetic fields due to spin–orbit coupling. In a simplest case, the local spin–orbit field $\mathbf{B}_{\text{eff}}$ may either augment or oppose an appropriately-directed applied field (say, B_y), shifting the peak of local Hanle data away from $B_y = 0$. In figure 5, we activate a spin–orbit coupling in a bulk epilayer of n:GaAs by applying, *in situ*, a uniaxial shear stress [20]. Uniform stress along the [011] GaAs crystal axis generates a spin–orbit coupling of the form $\epsilon_{xy}(\sigma_x k_y - \sigma_y k_x)$ (the same symmetry as Rashba spin–orbit coupling in heterostructures), where ϵ_{xy} is an off-diagonal element of the GaAs crystallographic strain tensor. For optically-injected spins diffusing radially away from the injection point, $\mathbf{B}_{\text{eff}}$ (as seen by the diffusing electrons) circulates around the point of injection.

Figure 5 shows images of optically-injected spins in a n:GaAs epilayer. The sample is unstrained in figure 5(a), while in figure 5(b) a small [011] uniaxial stress is applied, activating a spin–orbit coupling and a circulating effective field $\mathbf{B}_{\text{eff}}$, as drawn. In figure 5(b), the influence of $\mathbf{B}_{\text{eff}}$ on the diffusing spins is slight, but can be inferred from the slightly reduced spatial extent of the spin cloud. Figure 5(c) shows how the actual strain is measured via the induced blueshift of the GaAs bandedge (the 1 meV blueshift corresponds to an off-diagonal strain $\epsilon_{xy} = 1.5 \times 10^{-4}$) [20]. Figure 5(d) shows a conventional Hanle effect measurement using a large defocused pump spot. The spin lifetime in the unstrained epilayer (black trace), $\tau_s \simeq 210$ ns, is largely unaffected by this small strain (blue trace). These conventional Hanle curves are necessarily symmetric about zero applied field—the net momentum of the entire spin ensemble averages to zero, and therefore the average spin–orbit field is also zero. Only when the spin ensemble has a net momentum can these ordinary Hanle data develop asymmetries, and reveal an underlying spin–orbit coupling [28, 29]. This situation is shown explicitly in figure 5(e) for the case of conventional Hanle effect studies in a slightly (and unintentionally) strained epilayer. When laterally voltage-biased so that the injected spins have a net drift momentum $\mathbf{k}$ to the right or left ($\pm\hat{x}$), the peak of the Hanle curves shift to $B_y \simeq \pm 0.5$ G, respectively, indicating that $\mathbf{B}_{\text{eff}} \simeq 0.5$ G oriented along $\mp\hat{y}$.

In contrast, *local* Hanle effect studies using focused pump and probe beams can directly reveal spin–orbit effects without imparting a net $\mathbf{k}$ using external voltages. This is due to the fact that a local probe measures only a subset of the diffusing spin ensemble. Depending on the probe's position, this subset of spins can have a well-defined average momentum, $\mathbf{k}$, due to diffusion alone. Figure 6 shows local Hanle data acquired at several positions (see red dots) on either side of the radially-diffusing spin cloud, both before and after activating a spin–orbit coupling with uniaxial stress. In the unstrained case (figures 6(a)–(c)), local Hanle data on either side of the spin cloud (red and black traces) are identical and symmetric about $B_y = 0$.

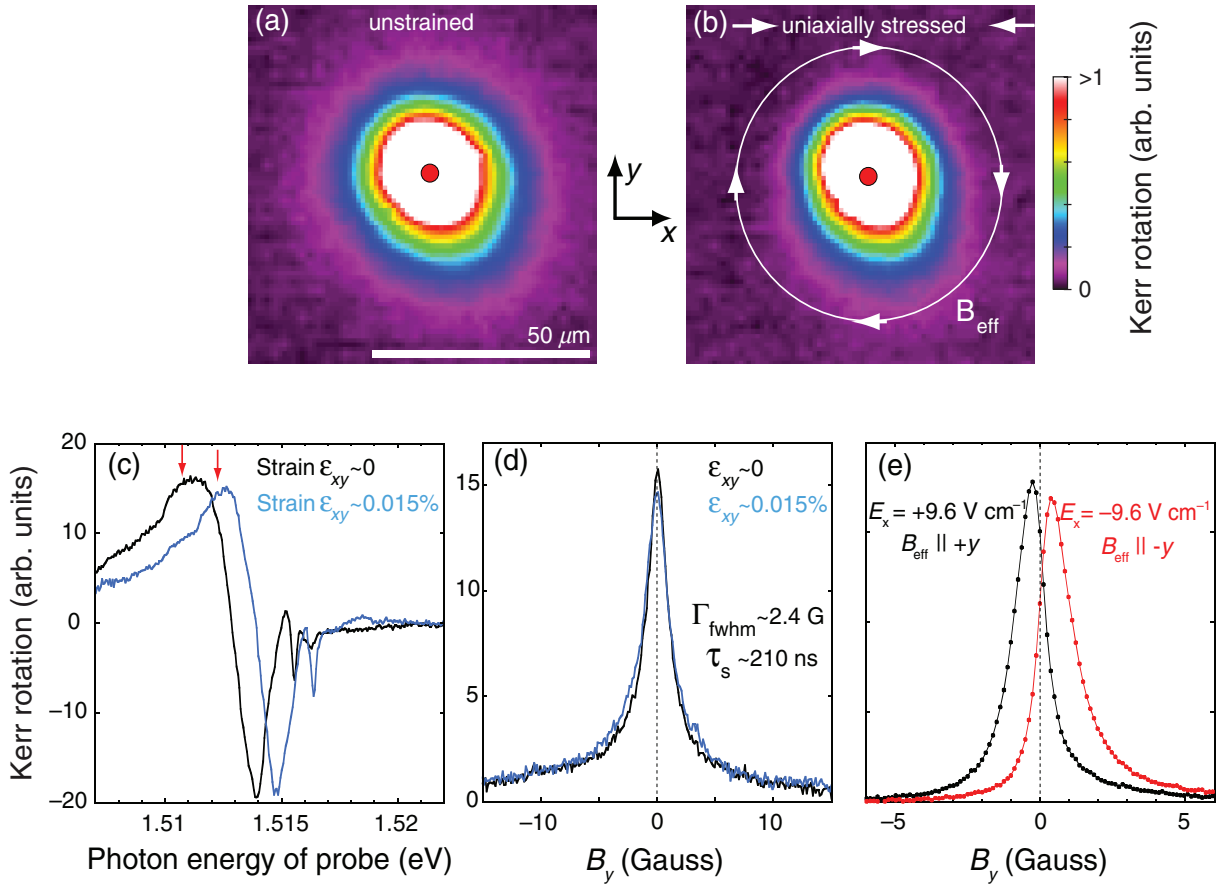

Figure 5. Images of spins diffusing radially away from the point of optical injection (red spot) in a n:GaAs epilayer ($n_e = 1 \times 10^{16}\,\mathrm{cm}^{-3}$) at 4 K, both (a) before and (b) after activating a spin–orbit coupling via a small uniaxial stress along [011]. (c) The induced strain ($\epsilon_{xy} = 0.015\%$) gives a 1 meV blueshift of the GaAs band-edge. Red arrows show the probe photon energy used for imaging and Hanle studies. (d) Conventional Hanle effect in this epilayer (S_z versus B_y, using a defocused pump spot). The spin lifetime, $\tau_s \simeq 210$ ns, is largely unaffected by this small strain. (e) Conventional Hanle effect data in a strained $n_e = 4 \times 10^{15}$ epilayer, where the injected spin ensemble drifts in a lateral electric field $E_x = \pm 9.6\,\mathrm{V\,cm}^{-1}$.

In marked contrast, data taken on either side of the spin cloud in the presence of this small strain (figures 6(e)–(g)) show clear asymmetries. Local Hanle data acquired to the left of the injection spot (red curves) are shifted to $-B_y$, while data acquired to the right of the injection spot (black) are shifted to $+B_y$. These studies indicate that the spin–orbit field $\mathbf{B}_{\mathrm{eff}}$ is oriented along $\pm y$ for spins diffusing along $\mp x$, respectively, consistent with $\mathbf{B}_{\mathrm{eff}}$ circulating around the point of injection as depicted in figure 5(b). Local Hanle measurements at additional points on the spin cloud confirm the chiral nature of $\mathbf{B}_{\mathrm{eff}}$ [20]. These position-dependent data can be accurately simulated (figures 6(d) and (h)), both with and without strain, by numerically solving the full set of 2D spin drift-diffusion equations.

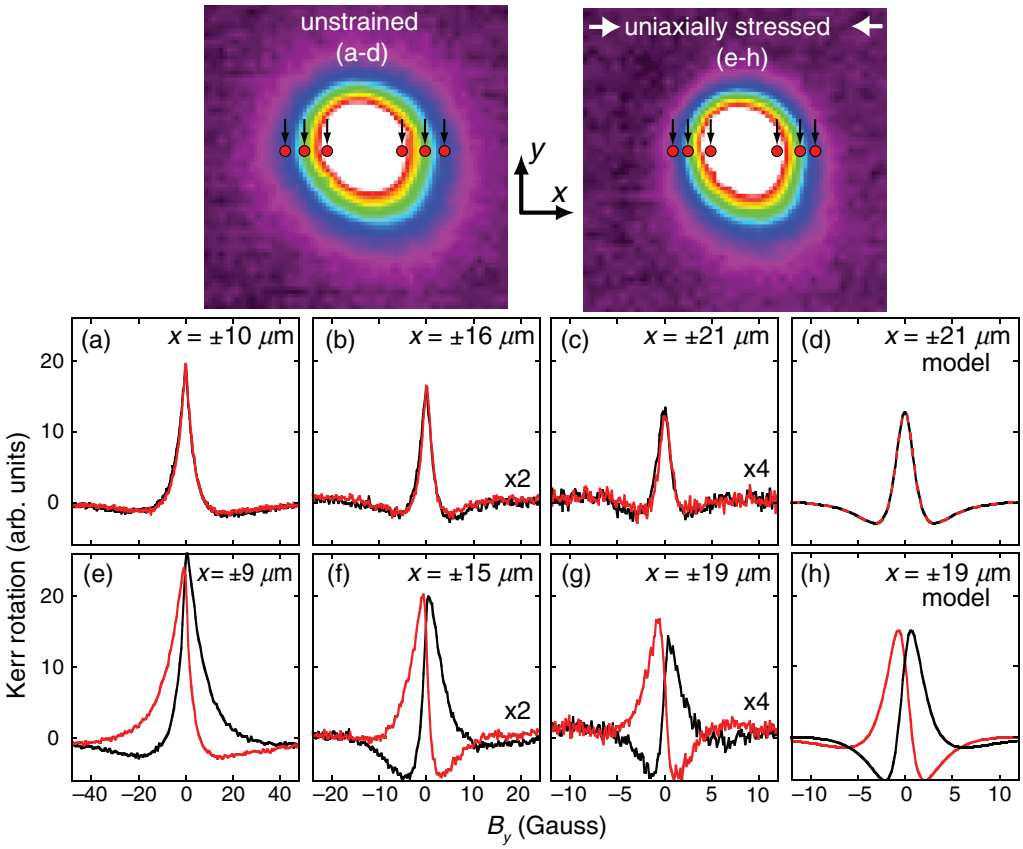

Figure 6. Local Hanle effect (S_z versus B_y, using focused pump/probe beams) measured at specific points on a radially diffusing spin cloud. (a)–(c) Local Hanle effect measured in zero strain at 10, 16, and 21 μm to the left (red) and right (black) of the injection spot (see points in image). Curves are symmetric about $B_y = 0$. (d) Simulated data at $\pm 21\,\mu$m in zero strain. (e)–(g) Local Hanle effect measured at 9, 15, and 19 μm to the left (red) and right (black) of the injection point in the presence of a spin–orbit coupling due to strain ($\epsilon_{xy} = 0.015\%$). Data show a marked asymmetry. (h) A simulated Hanle curve at $\pm 19\,\mu$m using $\epsilon_{xy} = 0.015\%$, $\tau_s = 210$ ns, and $D = 10\,\mathrm{cm}^2\,\mathrm{s}^{-1}$.

7. Local Hanle effect studies of spin drift and diffusion in Fe/GaAs devices

In this section, we use local Hanle effect studies to measure the drift and diffusion of spin-polarized electrons that are *electrically* injected into semiconductor devices. Motivated by the original notion of a 'spin transistor' [30], there is considerable interest in hybrid ferromagnet–semiconductor devices—particularly devices having a lateral channel and a field-effect geometry—that can be used to inject, manipulate and detect electron spins using an all-electrical scheme. Prototype structures have been fabricated and studied [9, 12, 31], but interpretation of electrical signals has often been subject to debate [32]. Complicating and often obscuring the spin-dependent electrical signals are extrinsic effects due to local Hall effects and contact magnetoresistance. For these reasons, scanning Kerr microscopy and local Hanle studies of spin flow in prototype ferromagnet–semiconductor devices are especially helpful in

interpreting electrical signals [10]. These optical data directly reveal the magnitude, sign and spatial extent of spin drift and diffusion in the device and are generally free from extrinsic electrical effects.

Figure 7(a) shows a photomicrograph of an all-electrical lateral injector *and* detector of spin-polarized electrons [12]. This device has five $10 \times 50\,\mu$m Fe/GaAs Schottky tunnel-barrier contacts (labeled 1–5) on a lateral n:GaAs channel. The heterostructure was grown by molecular beam epitaxy following [10, 12]. Briefly, 2500 nm of Si-doped n:GaAs ($n_e = 2.5 \times 10^{16}\,\mathrm{cm}^{-3}$) was grown on (100) semi-insulating GaAs. The doping was then increased to $n^+ = 5 \times 10^{18}\,\mathrm{cm}^{-3}$ over the next 15 nm, followed by a 15 nm layer doped at this high level. Fe (5 nm) was epitaxially deposited, followed by 2 nm of Al. The n^+:GaAs layers beneath the Fe define a narrow Schottky barrier through which electrons can tunnel [4]. Except for the regions defining the contacts, the Fe and n^+:GaAs were then etched away to define the lateral device. Gold vias deposited on a SiN isolation layer make electrical contact to the Fe. The easy-axis magnetization of the Fe contacts is oriented along the [011] GaAs crystal direction ($\pm\hat{y}$).

We focus on spin injection and spin extraction at contact 4. The dotted square in figure 7(a) shows the $65 \times 65\,\mu$m region around contact 4 that was imaged. The reflected probe power in this region (figure 7(b)) clearly shows contact 4, the n:GaAs channel, and the edges of the SiN layer. Under bias, the electron current, I_e, flows *within* the imaged region when electrons flow between contacts 4 and 5. In this case the electric field in the channel, E_x, is nonzero in the imaged region and the drift velocity $v_d = \mu E_x$ may either augment or oppose electron diffusion away from contact 4, depending on the direction of I_e. Conversely, when I_e flows between contacts 4 and 1, the current path is *outside* of the imaged region. In this case, E_x is nominally zero in the imaged region regardless of I_e, and spin transport in this region should be purely diffusive.

Figures 7(c)–(f) show the imaged spin polarization for the case of spin *injection* (i.e. the Fe/GaAs Schottky contact is reverse-biased and electrons flow from Fe into n:GaAs). In this device, *majority* spins (having spin orientation antiparallel to the Fe magnetization **M**) are injected for all reverse biases. The images show four cases: low or high electron drift velocity, with the current path within or outside of the imaged region. For clarity, contact 4 in these images is outlined by a dotted rectangle, and the black arrows indicate the direction and magnitude of the net electron current, I_e. In figure 7(c), electrons are injected at low reverse bias and they drift slowly to the right along $+\hat{x}$. The electron current $I_e^{4\to5} = 25\,\mu$A and the voltage across the Fe/GaAs interface is $V_{int} \simeq 53$ mV. Because the electrically-injected electrons have initial spin orientation in the plane of the device (along the Fe magnetization, $\mathbf{M} \parallel \pm\hat{y}$), a small transverse magnetic field $\pm B_x$ is used to tip (precess) these spins out-of-plane (along $\pm\hat{z}$) so that S_z can be measured by the polar Kerr effect [10]. All the images in figures 7 and 8 show the difference between Kerr images acquired at $B_x = +2.4$ and -2.4 G. In this way, field-independent backgrounds are subtracted off, and only the signal that depends *explicitly* on electron spin precession remains. Figure 7(c) clearly shows a cloud of spin-polarized electrons emerging from and flowing away from contact 4, with an apparent spatial extent of order 20 μm in the n:GaAs channel (note that the apparent extent of S_z in these images depends on B_x [33]). In this case, both drift and diffusion drive a net flow of spins to the right.

A remarkably similar image is observed, however, when spins are injected out of contact 4 under similar bias conditions ($I_e^{4\to1} = 25\,\mu$A) but are drifting to the *left*, along $-\hat{x}$ (figure 7(d)). In this case the current path is outside the imaged region, and E_x in the imaged region is nominally zero. The cloud of spins seen to the right of contact 4 are those spins that have

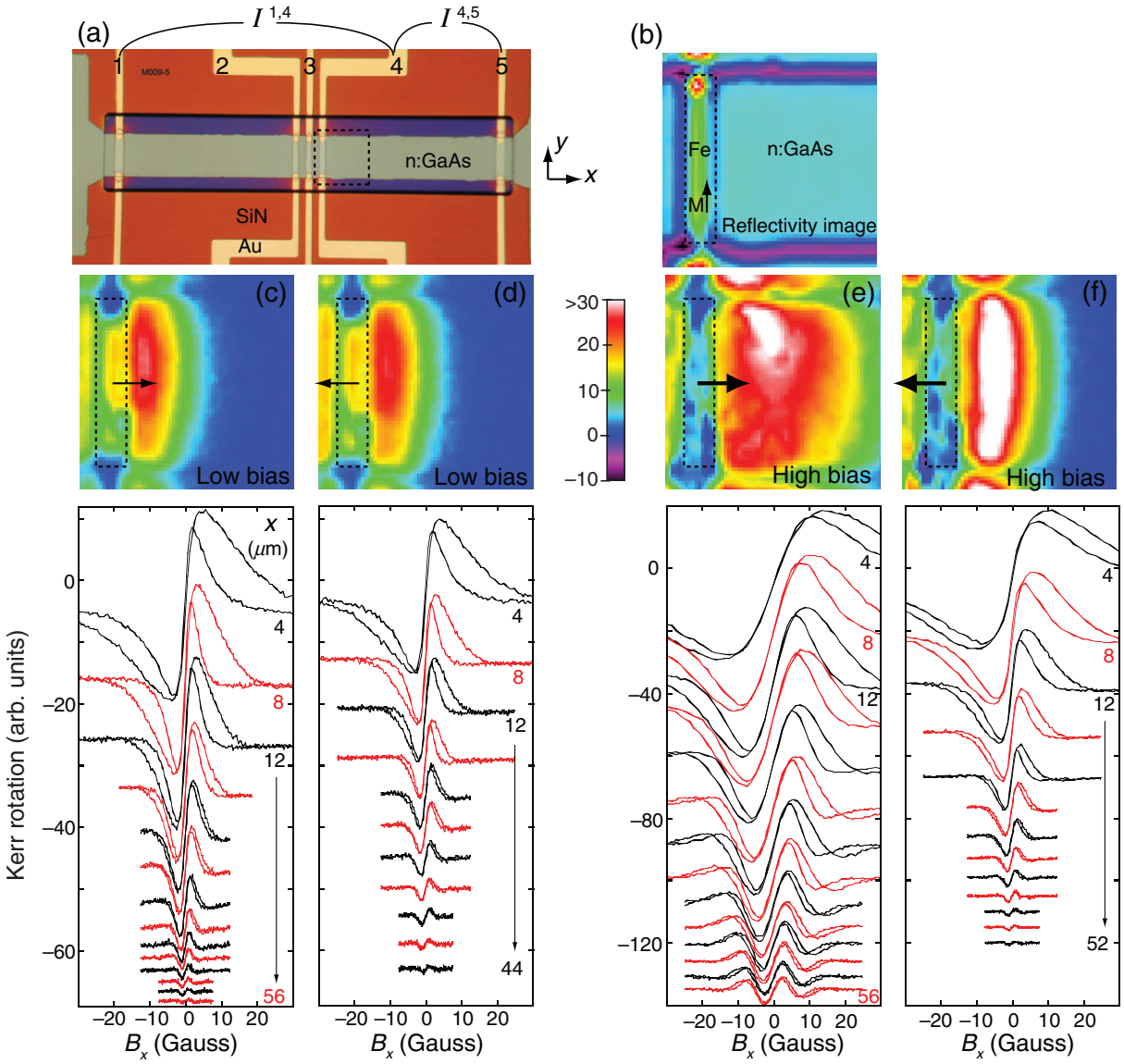

Figure 7. (a) A spin transport device with five Fe/GaAs contacts (#1–5). A $65 \times 65\,\mu$m region around contact 4 is imaged (dotted square). (b) The reflected probe power in this region, showing device features. (c)–(f) Images of the electrically-injected spin polarization ($B_x = 2.4$ G, tipping injected spins into $\hat{z}$). Arrows show the direction and magnitude of net electron current, I_e. (c) Spins are injected at low bias ($I_e^{4\to5} = 25\,\mu$A) and drift/diffuse to the right. (d) Spins are injected at low bias and drift to the *left* ($I_e^{4\to1} = 25\,\mu$A); the spins to the right of contact 4 have diffused away from the current path. (e, f) Similar images at higher bias ($I_e = 125\,\mu$A). Lower images are the local Hanle data (S_z versus B_x) at different distances from contact 4.

diffused out from under the contact, and which are now flowing to the right due to diffusion alone. The similarity of both the magnitude and the spatial extent of S_z in figures 7(c) and (d) suggests that drift plays only a minor role in determining the overall transport of spins under these low-bias conditions.

Local Hanle data confirm this. The actual spatial decay of the injected spin polarization can be inferred from the series of local Hanle curves (S_z versus B_x) shown below each image. Numbers indicate the separation, in microns, between the right edge of contact 4 and the detection spot. Because the injected spin orientation is in-plane (along $\hat{y}$, as opposed to along $\hat{z}$ for optical injection), the local Hanle curves have an antisymmetric shape. Small transverse fields $\pm B_x$ cause injected spins to precess into $\pm\hat{z}$, giving positive and negative θ_K and an antisymmetric lineshape. In the data shown, B_x was swept from negative to positive and back to negative values ($|B_x| < 50$ G), and both up- and down-sweeps are shown. Some hysteresis is evident near the contact, likely resulting from some nuclear spin polarization in the n:GaAs generated by the hyperfine interaction with spin-polarized electrons [34]. The peak-to-peak amplitude of the local Hanle data provides a measure of the net spin polarization in the n:GaAs channel (the decay of these amplitudes will be summarized in figure 9). In both figures 7(c) and (d), the spin polarization in the n:GaAs channel to the right of contact 4 falls with a $1/e$ decay length of $\sim$11 μm—the spin diffusion length in this device. Note that the peak-to-peak width of the data also drops with increasing distance, reflecting the increased age of the spins that are measured by the probe beam.

In contrast, the effects of spin drift *are* readily apparent when E_x in the channel is larger. Figure 7(e) shows spin injection from contact 4 under high bias conditions ($I_e^{4\to5} = 125\,\mu$A, $V_{int} \simeq 200$ mV), with electrons drifting to the right. The apparent extent of the injected spin cloud is much longer as compared with figure 7(c). The peak-to-peak amplitudes of the local Hanle data shown below the image indicate a much longer decay length of $\sim$22 μm. Furthermore, the local Hanle curves at any given distance from contact 4 are significantly wider under high-bias conditions, reflecting the shorter time required for the electrons to travel from the contact to the point of detection. Finally, the local Hanle curves at large distance show clear time-of-flight oscillations, which can be used to measure $v_d \simeq 3.5 \times 10^4$ cm s^{-1}. Alternatively, figure 7(f) shows injected spins when the high-bias current path lies *outside* the imaged region ($I_e^{4\to1} = 125\,\mu$A). The apparent extent of S_z is shorter and in keeping with diffusive spin transport. The local Hanle data indicate a spatial decay of 11 μm, as seen previously in figures 7(c) and (d), for the case of low bias and predominantly diffusive transport.

In addition to electrical spin injection from a ferromagnet into a semiconductor, previous studies [10, 15] have also shown that a spin polarization can accumulate when electrons are extracted from a semiconductor into a ferromagnetic contact at a forward-biased Schottky contact. Figure 8 shows the corresponding set of images and local Hanle studies for the case of spin accumulation due to spin extraction in this Fe/GaAs device. The same $65\times65\,\mu$m region near contact 4 is imaged. Here, the spin-dependent transmission of electrons tunneling from n:GaAs into contact 4 leaves an accumulation in the channel of spins belonging to the less-transmissive state. This spin polarization diffuses out from under the contact, either into the current path (where drift now *opposes* diffusion), or outside of the current path (where spins diffuse freely). The four images in figure 8 show both cases, at both low and high drift velocity.

Figures 8(a) and (b) show spin accumulation due to spin extraction both within and outside of the current path under low forward bias conditions ($I_e^{5\to4} = I_e^{1\to4} = 25\,\mu$A). In both cases, the apparent spatial extent of the accumulated S_z is similar to the case of purely diffusive spin transport. The local Hanle data confirm this, showing decay lengths of order 11 and 12 μm, respectively. (Note that the sign of the accumulated spin polarization is oppositely-oriented in figures 8(a) and (b)—in this particular device, *minority* spin polarization accumulates at

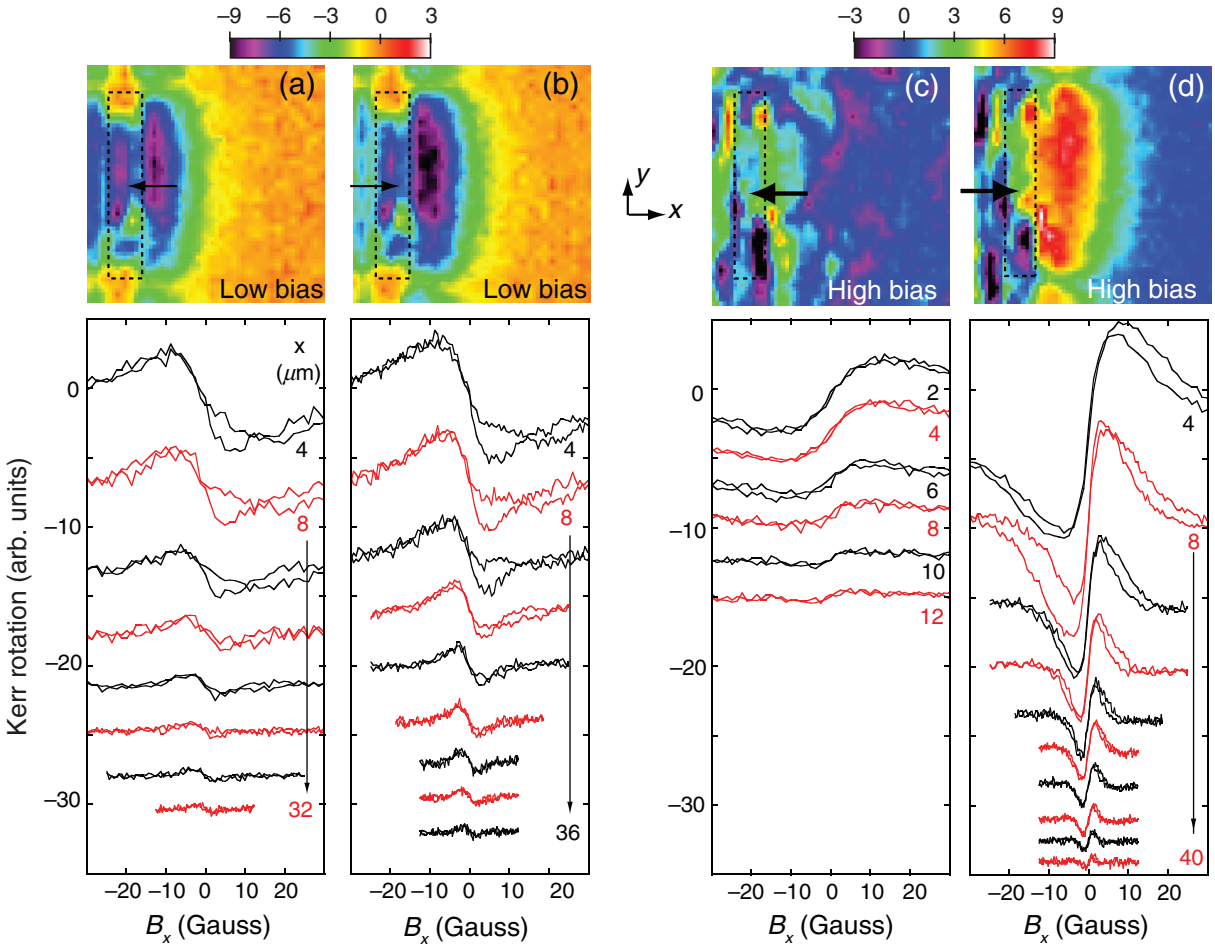

Figure 8. 65 × 65 μm Kerr images (and local Hanle data) for spin accumulation due to spin *extraction* near contact 4 (i.e. electrons flow from n:GaAs into Fe). Arrows indicate the direction and magnitude of the net electron current, I_e. (a) and (b) correspond to low electron drift velocity ($I_e = 25\,\mu$A). Note that the accumulated spin polarization has opposite sign at low contact bias. (c) and (d) correspond to high drift velocity ($I_e = 125\,\mu$A).

low forward biases, as described in a previous study [12]). In contrast, dramatic differences are clearly seen between figures 8(c) and (d) when the drift current is large ($I_e = 125\,\mu$A). Figure 8(c) shows that accumulated spins cannot diffuse very far against I_e; the polarization decays within 5 μm from the edge of contact 4. Alternatively, if the current path lies outside the imaged region (figure 8(d)), then accumulated spins diffuse freely to the right of contact 4 with the diffusion length in this device.

Spin drift and diffusion in these Fe/GaAs devices are summarized in figure 9, which shows the peak-to-peak amplitudes of the local Hanle data plotted as a function of distance from contact 4. The contact is shown by the green bar, and arrows denote both the direction and magnitude of the electron current I_e. For clarity, the current path is always depicted as being to the right of the contact, so that diffusive spin flow away from the current path always appears to the left of the contact. The differences in overall magnitude of S_z between low

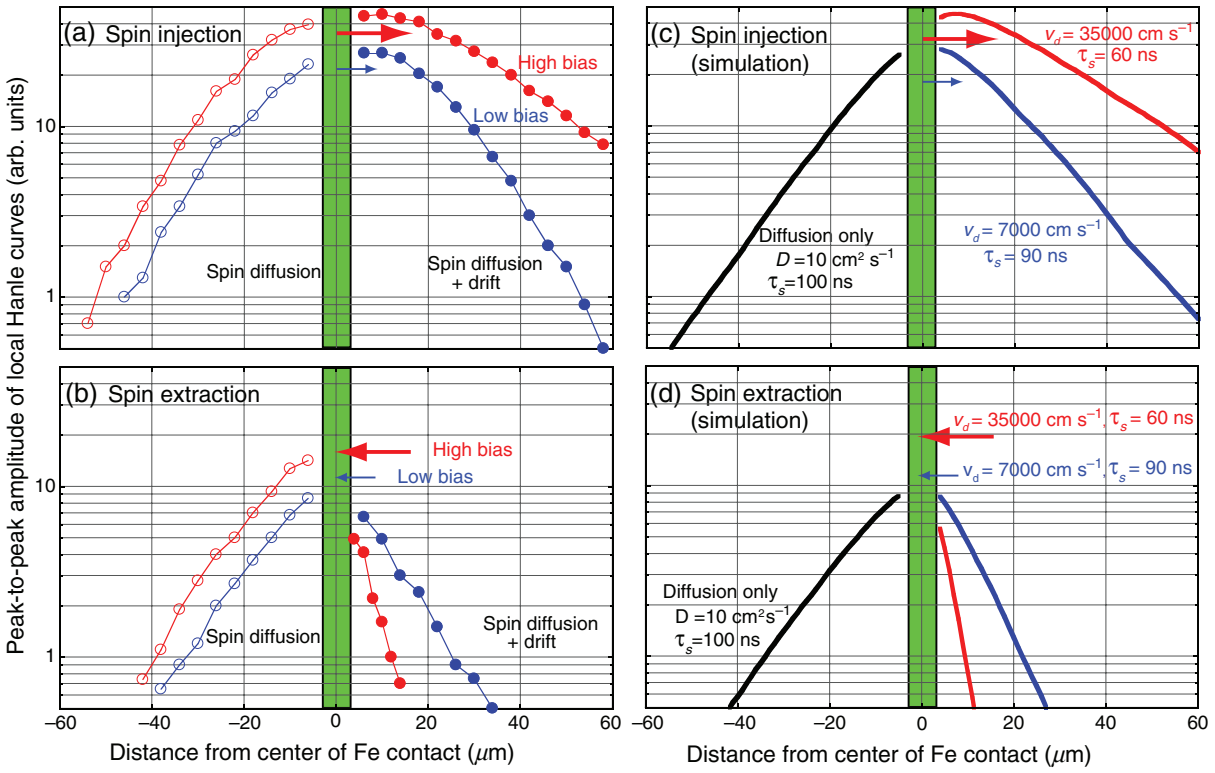

Figure 9. (a) Summarizing the peak-to-peak amplitudes of the local Hanle data shown in figure 7. These amplitudes provide a measure of the electron spin polarization in the n:GaAs channel versus distance from the Fe/GaAs contact (denoted by the green region). Arrows indicate the direction and magnitude of electron drift. Blue and red data points were acquired under low and high drift velocity conditions, respectively ($I_e = 25, 125\,\mu$A). Filled (open) symbols indicate data taken within (outside of) the current path. This plot shows data for the case of spin *injection* (reverse-biased Fe/GaAs contact; electrons flowing from Fe to GaAs). (b) The same, but for the case of spin polarization due to spin *extraction* shown in figure 8 (forward-biased contact, or electrons flowing from GaAs into Fe). (c) and (d) Amplitudes of simulated local Hanle data.

and high bias conditions (or between injection and extraction) are due to the bias-dependent injection/extraction efficiency of these Fe/GaAs contacts [12]. Several features are notable: (i) at low bias, spins on either side of the contact (both within the current path, or outside of it) show similar 11–12 μm decays. In this case, spin drift plays a relatively minor role compared to diffusion. As expected, this holds true whether the spin polarization is due to injection or extraction. (ii) Spin transport outside of the current path is always diffusive, regardless of the biasing conditions. This agrees with the expectation that E_x outside of the current path is nominally zero. (iii) Large spin drift currents can markedly augment or suppress the natural diffusion of spins, depending on the drift direction. This is in contrast with all-metal spin-transport devices, where diffusion generally dominates drift effects [35].

Figures 9(c) and (d) show peak-to-peak amplitudes of simulated local Hanle data. Outside the current path, the spatial decay determines the diffusion length $\sqrt{D\tau_s}$. τ_s (which decreases

with bias [25]) is measured independently using a defocused pump beam, and equals 100 ns in this structure at zero bias. We therefore set $D = 10\,\mathrm{cm}^2\,\mathrm{s}^{-1}$. The drift velocity v_d is then chosen to fit the spatial decay of spin polarization in the current path at finite bias, and good agreement is found when $v_\mathrm{d} = 3.5$ and $0.7 \times 10^4\,\mathrm{cm\,s}^{-1}$ for high and low bias, respectively. These data directly aid in the design of all-electronic spintronic devices. For example, these local Hanle data clearly show that electrical spin-detection electrodes in this structure may be located within ∼10–20 μm of a spin-injection contact without significant loss of expected signal, either within—or outside of—the current path. Further, the relative magnitude (and sign) of anticipated electrical signals as a function of applied **E** and **B** fields are also revealed by these local Hanle studies, lending confidence to the interpretation of spin-dependent electrical signals [12].

8. Conclusions

In conclusion, we have shown how local Hanle-effect studies of spatially-dependent electron depolarization assist in determining important spin transport parameters such as drift velocity, diffusion constant, mobility and spin lifetime. In n:GaAs epilayers and hybrid spin transport devices, these measurements provide a relatively complete picture of the drift and diffusion of both optically or electrically injected spins, particularly when used in conjunction with direct images of the 2D spin distribution. Analytic solutions to the 2D spin drift-diffusion equations are presented for the general case of in-plane electric and magnetic fields, and a numerical solution is outlined if spin–orbit effects are also present. The effective magnetic fields due to spin–orbit coupling manifest directly in the local Hanle data when the local probe selectively pinpoints subsets of the spin distribution that have finite momentum. In lateral Fe/GaAs spin injection and detection devices, local Hanle studies reveal the spin transport parameters both within and outside of the current path. These data are used to guide the design of all-electrical spin transport devices.

Acknowledgments

We thank X Lou for assistance with sample processing, and acknowledge support from the DARPA SpinS and the Los Alamos LDRD programs, the NSF MRSEC program under grant DMR 02-12302, the Office of Naval Research, and the Minnesota Nanofabrication Center, which is supported by the NSF National Nanotechnology Infrastructure Network. EG was supported by an NSF IGERT fellowship.

References

[1] Fiederling R, Keim M, Reuscher G, Ossau W, Schmidt G, Waag A and Molenkamp L W 1999 *Nature* **402** 787
[2] Ohno Y, Young D K, Beschoten B, Matsukura F, Ohno H and Awschalom D D 1999 *Nature* **402** 790
[3] Zhu H J, Ramsteiner M, Kostial H, Wassermeier M, Schonherr H P and Ploog K H 2001 *Phys. Rev. Lett.* **87** 016601
[4] Hanbicki A T, Jonker B T, Itskos G, Kioseoglou G and Petrou A 2002 *Appl. Phys. Lett.* **80** 1240
[5] Motsnyi V F, De Boeck J, Das J, Van Roy W, Borghs G, Goovaerts E and Safarov V 2002 *Appl. Phys. Lett.* **81** 265

[6] Jiang X, Wang R, Shelby R M, Macfarlane R M, Bank S R, Harris J S and Parkin S S P 2005 *Phys. Rev. Lett.* **94** 056601
[7] Adelmann C, Lou X, Strand J, Palmstrøm C J and Crowell P A 2005 *Phys. Rev.* B **71** 121301
[8] Moser J *et al* 2006 *Appl. Phys. Lett.* **89** 162106
[9] Hammar P R and Johnson M 2002 *Phys. Rev. Lett.* **88** 066806
[10] Crooker S A, Furis M, Lou X, Adelmann C, Smith D L, Palmstrøm C J and Crowell P A 2005 *Science* **309** 2191
[11] Lou X, Adelmann C, Furis M, Crooker S A, Palmstrøm C J and Crowell P A 2006 *Phys. Rev. Lett.* **96** 176603
[12] Lou X, Adelmann C, Crooker S A, Garlid E S, Zhang J, Reddy K S M, Flexner S D, Palmstrøm C J and Crowell P A 2007 *Nat. Phys.* **3** 197
[13] Žutić I, Fabian J and Das Sarma S 2004 *Rev. Mod. Phys* **76** 323
[14] Kato Y, Myers R C, Gossard A C and Awschalom D D 2004 *Nature* **427** 50
[15] Stephens J, Berezovsky J, McGuire J P, Sham L J, Gossard A C and Awschalom D D 2004 *Phys. Rev. Lett.* **93** 097602
[16] Weber C P, Gedik N, Moore J E, Orenstein J, Stephens J and Awschalom D D 2005 *Nature* **437** 1300
[17] Couto O D D, Iikawa F, Rudolph R, Hey R and Santos P V 2007 *Phys. Rev. Lett.* **98** 036603
[18] Dyakonov M I and Perel V I 1984 *Optical Orientation* ed F Meier and B Zakharchenya (Amsterdam: North-Holland) p 39
[19] Kikkawa J M and Awschalom D D 1999 *Nature* **397** 139
[20] Crooker S A and Smith D L 2005 *Phys. Rev. Lett.* **94** 236601
[21] Hruška M, Kos S, Crooker S A, Saxena A and Smith D L 2006 *Phys. Rev.* B **73** 075306
[22] Pikus G E and Titkov A N 1984 *Optical Orientation* ed F Meier and B Zakharchenya (Amsterdam: North-Holland) p 80
[23] Dzhioev R I, Kavokin K V, Koronev V I, Lazarev M V, Meltser B Y, Stepanova M N, Zakharchenya B P, Gammon D and Katzer D S 2002 *Phys. Rev.* B **66** 245204
[24] Dzhioev R I, Koronev V L, Merkulov I A, Zakharchenya B P, Gammon D, Efros Al L and Katzer D S 2002 *Phys. Rev. Lett.* **88** 256801
[25] Furis M, Smith D L, Crooker S A and Reno J L 2006 *Appl. Phys. Lett.* **89** 102102
[26] Flatté M E, Byers J M and Lau W H 2002 *Semiconductor Spintronics and Quantum Computation* ed D D Awschalom, D Loss and N Samarth (Berlin: Springer) p 107
[27] Winkler R 2003 *Spin-orbit Coupling Effects in 2D Electron and Hole Systems* (Berlin: Springer)
[28] Kalevich V K and Korenev V L 1990 *JETP Lett.* **52** 230
[29] Sih V, Knotz J, Stephens J, Horowitz V R, Gossard A C and Awschalom D D 2006 *Phys. Rev.* B **73** 241316
[30] Datta S and Das B 1990 *Appl. Phys. Lett.* **56** 665
[31] Hammar P R, Bennett B R, Yang M J and Johnson M 1999 *Phys. Rev. Lett.* **83** 203
[32] Tang H X, Monzon F G, Jedema F J, Filip A T, van Wees B and Roukes M L 2002 *Semiconductor Spintronics and Quantum Computation* ed D D Awschalom, D Loss and N Samarth (Berlin: Springer) p 31
[33] Crooker S A, Furis M, Lou X, Crowell P A, Smith D L, Adelmann C and Palmstrom C J 2007 *J. Appl. Phys.* **101** 081716
[34] Paget D, Lampel G, Sapoval B and Safarov V I 1977 *Phys. Rev.* B **15** 5780
[35] Jedema F J, Heersche H B, Filip A T, Baselmans J J A and van Wees B J 2002 *Nature* **416** 713